Infrared frequency comb generation and spectroscopy with suspended silicon nanophotonic waveguides

Nima Nader,[1,*] Abijith Kowligy,[2,†] Jeff Chiles,[1,†] Eric J. Stanton,[1] Henry Timmers,[2] Alexander J. Lind,[2,3] Flavio C. Cruz,[2,4] Daniel M. B. Lesko,[2,3] Kimberly A. Briggman,[1] Sae Woo Nam,[1] Scott A. Diddams,[2,3,5] and Richard P. Mirin[1,6]

[1]Applied Physics Division, National Institute of Standards and Technology, 325 Broadway, Boulder, Colorado 80305, USA
[2]Time and Frequency Division, National Institute of Standards and Technology, 325 Broadway, Boulder, Colorado 80305, USA
[3]Department of Physics, University of Colorado, 2000 Colorado Avenue, Boulder, Colorado 80309, USA
[4]Instituto de Fisica Gleb Wataghin, Universidade Estadual de Campinas, Campinas, SP, 13083-859, Brazil
[5]e-mail: scott.diddams@nist.gov
[6]e-mail: richard.mirin@nist.gov
*Corresponding author: nima.nader@nist.gov

Nanophotonic waveguides with sub-wavelength mode confinement and engineered dispersion are an excellent platform for application-tailored nonlinear optical interactions at low pulse energies. We present fully air-clad suspended silicon waveguides for infrared frequency comb generation with optical bandwidth limited only by the silicon transparency. Precise lithographic control over the waveguide dispersion enables tailored infrared frequency comb generation across a bandwidth of 2.0–8.8 µm (1130–5000 cm^{-1}), with the broadest simultaneous bandwidth covering 2.0–7.7 µm. Novel fork-shaped couplers provide efficient input coupling with only 1.5 dB loss. The coherence, brightness, and stability of the generated light are highlighted in a dual-frequency comb setup in which individual comb lines are resolved with 30 dB extinction ratio and 100 MHz spacing in the wavelength range of 4.9–8.8 µm (1130–2050 cm^{-1}) using three different waveguide widths. These sources are used for broadband gas- and liquid-phase dual-comb spectroscopy with 100 MHz comb line resolution. We achieve a peak spectral signal-to-noise ratio of 10 $\sqrt{\text{Hz}}$ across a simultaneous bandwidth of 6.3–8.2 µm (1220–1590 cm^{-1}) containing 112,200 comb lines. These results provide a pathway to further integration with the developing high-repetition-rate frequency comb lasers for compact sensors with applications in chip-based chemical analysis and spectroscopy.

1. INTRODUCTION

Nanophotonic waveguides offer sub-wavelength mode confinement with effective modal area of ∼1 µm^2. This enhances the nonlinear optical interactions significantly and enables efficient wavelength conversion at low pulse energies. Subsequently, this results in the reduction of size, complexity, and power consumption of nonlinear optical systems. Moreover, the recent development of compact mode-locked lasers [1–3] with repetition rates, f_{rep}, on the order of 1–10 GHz has increased the demand for integrated on-chip nonlinear devices operating at low pulse energies. Photonic waveguides pumped with picojoule-level pulses are used for self-referencing of frequency combs through carrier-offset frequency (f_0) detection and stabilization [4–7].

Optical frequency combs are phase-stabilized mode-locked lasers with broadband spectra of discrete, narrow optical lines spaced by the f_{rep} [8–11]. These are excellent sources for precision metrology and spectroscopy applications [12] where octave

spanning, high-coherence infrared (IR) spectral coverage is desired [13,14]. Such sources access the molecular rovibrational states with resonant absorption lines unique to each molecule within the mid-IR (3–5 µm) [15–18] and molecular fingerprinting regions (6–20 µm) [19,20]. These advantages enable coherent probing of multiple rovibrational transitions in gas and condensed phases with an unprecedented frequency accuracy. Such lasers, implemented in the form of low-cost on-chip platforms, have applications as portable and mobile sensors for in-lab analysis and fieldable trace chemical monitoring [21].

In this paper, we utilize fully air-clad suspended Si waveguides [22,23] for IR frequency comb generation. Si benefits from a broad transparency window of 1.1–8.8 µm and a high nonlinear index, n_2 (∼100× that of silica) [24,25]. The mature Si infrastructure enables reliable fabrication of versatile waveguides suitable for on-chip efficient $\chi^{(3)}$ nonlinear processes. Pumping waveguides with 100 pJ, 85 fs pulses at 3.06 µm, we generate IR spectra with 1–2 mW average powers. Precise lithographic control over the

geometrical dispersion enables spectral tailoring across >2.1 octaves, spanning 2.0–8.8 μm (1130–5000 cm^{-1}) by changing the waveguide width. Using suspended Si waveguides, we construct a dual-comb spectroscopy (DCS) setup for gas and liquid-phase sensing. Different waveguide widths enable measuring ~2.7 × 10^5 comb lines that span 4.9–8.8 μm (1130–2050 cm^{-1}), providing 100 MHz (0.0033 cm^{-1}) spectral resolution. The broadest simultaneous dual-comb bandwidth spans 4.9–8.0 μm with 2.5 × 10^5 comb lines. We study atmospheric water absorption with the 100 MHz comb line resolution and broadband absorption spectra of liquid-phase methanol and isopropanol. The smooth waveguide spectrum enables broadband baseline correction to realize excellent agreement with Fourier transform infrared (FTIR) measurements.

This work improves the current state-of-the-art on-chip mid-IR frequency comb generation [26–33] to realize picojoule-scale pulse energy and extend the spectral bandwidth to 8.8 μm, with milliwatt-scale average power and a DCS figure-of-merit (FOM) equivalent to other mid-IR dual-comb systems.

2. WAVEGUIDE DESIGN AND FABRICATION

Silicon photonics is predominantly focused on telecom applications based on the silicon-on-insulator (SOI) material platform. It is, however, challenging to realize high-performance nonlinear devices, mainly due to two-photon absorption (TPA) when waveguides are pumped below the TPA cutoff of 2.2 μm. In addition, the SiO$_2$ cladding has absorption at wavelengths >3.5 μm, limiting the utility of this platform in IR applications [26–28]. A number of alternative approaches have been investigated based on modified cladding materials to reduce IR absorption in conjunction with longer-wavelength pump sources to eliminate the TPA. In particular, Si-on-sapphire waveguides pumped above the TPA cutoff [34–36] have shown promising results, but have a long wavelength limit of 6 μm due to the sapphire absorption. Recently, SiGe-on-Si and chalcogenide-glass waveguides [37–39] have been introduced as new platforms for supercontinuum generation, reaching wavelengths >8.0 μm. These demonstrations are promising due to their large IR transparency windows.

We design and fabricate 5 mm long suspended Si waveguides based on 700 nm thick fusion-bonded Si membranes [22] for supercontinuum generation [Figs. 1(a) and 1(b)]. Removing the absorptive cladding eliminates the need for large cross-section waveguides to achieve low propagation losses in the IR [40], and enables access to the full transparency of Si. Moreover, this platform enables group-velocity-dispersion (GVD) engineering of the waveguides [23] to realize application-tailored spectra through coherent dispersive wave generation. The bonded Si membrane is provided by a SOI wafer, and the air trenches underneath the waveguides [Fig. 1(b)] are etched in a blank Si wafer prior to bonding (see Supplement 1 for the fabrication details). The dimensions of the trenches are designed to avoid leakage loss of the generated IR light. The waveguides are formed by partial etching of the Si membrane with etch depth of 390 nm, leaving a slab thickness of 310 nm to achieve the desired dispersion profiles for our nonlinear processes.

We implement floating fork-shaped couplers for efficient input [Figs. 1(c) and 1(d)] and output [Figs. 1(e) and 1(f)] coupling between the waveguide chip and the free-space mode. We use 3D finite-difference time-domain (FDTD) simulations to design the couplers with two symmetrical arms to couple the free-space
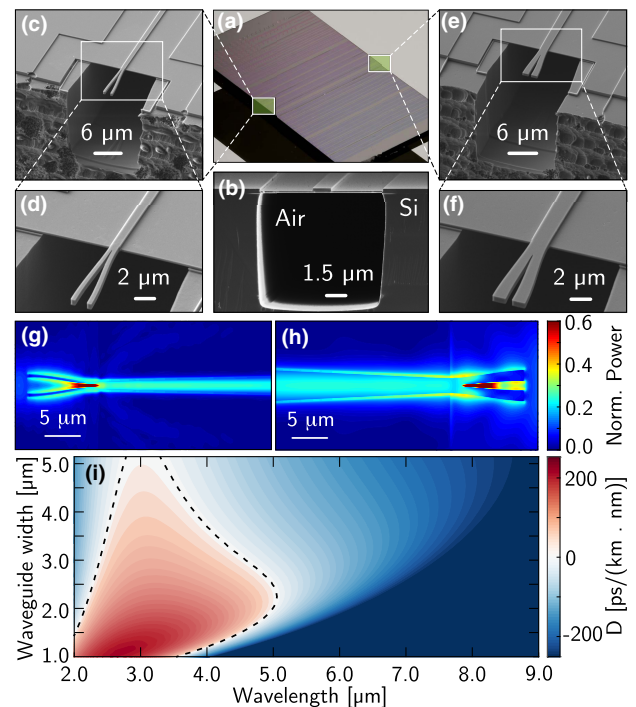

Fig. 1. Fabricated suspended Si waveguides. (a) Image of the fabricated suspended Si chip with scanning electron micrograph (SEM) of (b) the suspended waveguide cross section; (c), (d) the input; and (e), (f) the output fork-shaped couplers. Simulated electric-field wavefront transformation as the (g) 3.06 μm input and (h) 8.0 μm output modes propagate along the fork-shaped couplers. (i) The designed GVD of the waveguides plotted as a function of the wavelength for different waveguide widths. The geometrical dispersion of the waveguides can be tailored to provide GVD zero-crossing at different wavelengths (dashed line), providing the phase matching for dispersive wave generation.

mode to two points at the coupler tips [Figs. 1(g) and 1(h)]. As the two arms merge, the optical field is confined into the narrow gap in between. This enables fast compression of the free-space mode into the waveguide in a ~10–20 μm coupler length scale. Through FDTD simulations, widths of the coupler tips and their center-to-center gap can be designed to set the mode-field diameter of the expanded waveguide mode for optimized mode-matching to free space. The next design feature is the tapering of the widths of both arms from the tip to the point where they merge to preserve the adiabatic operation of the couplers. The compactness of these structures offers a significant advantage over conventional inverse tapers (with length-scales of hundreds of micrometers) for suspended photonics platforms, where mechanical stability places strong constraints on the dimensions of edge couplers. Moreover, the short coupler length facilitates removal of the slab in the coupler region without loss of mechanical stability. Such floating sections can be used for controlled waveguide mode expansion in both the horizontal and vertical directions, which in turn improves the coupling efficiency when compared to inverse tapers where the remaining waveguide slab limits the vertical mode expansion [41].

We form the couplers by full etching of the 700 nm thick suspended Si membrane. To reduce bend-to-straight waveguide transition losses at short length scales [Figs. 1(g) and 1(h)], a Bézier-type curvature is used to define the shape of the

arms [42,43]. The widths of the input and output taper tips are chosen as 440 nm and 1.4 µm, and they taper to 440 and 900 nm in a floating length of 10 µm. The center-to-center gaps are also designed as 1.86 and 2.2 µm for input and output couplers, respectively. We measure the best input coupling efficiency of 1.50 ± 0.13 dB/coupler at the 3.06 µm pump wavelength, which is in excellent agreement with the simulated value of 1.43 dB/coupler. The output coupler is designed for broadband operation in 6.0–8.8 µm range with ~3 dB efficiency.

The high core–cladding index contrast of 3.4:1.0 in suspended Si waveguides enables versatile geometrical GVD engineering with flat anomalous dispersion at the pump wavelength. The calculated GVD of the waveguides is presented in Fig. 1(i) as a function of wavelength for different waveguide widths. The plotted range of widths has anomalous dispersion at the pump wavelength, making the waveguides suitable for soliton fission and broadband coherent supercontinuum generation. Moreover, the long-wavelength zero-dispersion wavelength (ZDW) can be tailored from 3.5 to 5.0 µm by varying the waveguide width, providing the phase-matching condition for lithographically engineered dispersive wave generation in the IR.

For supercontinuum generation experiments, we use a mid-IR laser with 85 fs pulses centered at 3.06 µm, operating with 100 MHz repetition rate [pump spectrum in Fig. 2(a)]. This source is based on a 1550 nm Er:doped oscillator and difference-frequency-generation (DFG) in a periodically poled lithium niobate (PPLN) crystal [44]. We couple the free-space beam of the laser to the TE₀ mode of the waveguides using a mid-IR $Ge_{28}Sb_{12}Se_{60}$ aspheric lens with numerical aperture of 0.56. The output is collected using a 0.82 numerical aperture lens and monitored with an InSb camera to optimize the alignment. The output lens is aligned to maximize the coupling for the section of the spectrum at wavelengths >5.0 µm, and the collected supercontinuum spectra are recorded with an FTIR [Fig. 2(a)].

Pumping the waveguides at 3.06 µm avoids TPA, and the nonlinear FOM increases compared with the TPA-limited value. Nonlinear FOM is a metric to calculate the tradeoff between the nonlinearity of the medium, i.e., waveguides, and the nonlinear absorption. This parameter is defined as $n_2/\lambda\beta_{TPA}$ and $n_2/\lambda I\beta_{3PA}$ for TPA and three-photon-absorption (3PA), respectively [45]. Here, β_{TPA} and β_{3PA} are TPA and 3PA coefficients, respectively; λ is the pump wavelength and I is the light intensity inside the waveguide, defined as $I = P_p/A_{eff}$, with A_{eff} being the modal effective area at the pump wavelength and P_p being the coupled peak power. For the TPA-limited case $\lambda = 1550$ nm, $\beta_{TPA} \approx 0.51$ cm/GW and $n_2 \approx 2.5 \times 10^{-5}$ cm²/GW, which leads to the TPA-limited nonlinear FOM of ~0.3 [46]. We operate at the 3PA regime with $\lambda = 3.06$ µm, $\beta_{3PA} \approx 1.75 \times 10^{-3}$ cm³/GW², and $n_2 \approx 2.5 \times 10^{-5}$ cm²/GW [25]. We couple 100 pJ pulses (coupled peak power, $P_p = 1.1$ kW) to the suspended Si waveguides with typical $A_{eff} \approx 2$ µm². This gives the coupled peak intensity of $I = 59$ GW/cm². In this case, the 3PA nonlinear FOM is calculated as ~0.85, which is ~2.8× improvement over the TPA-limited value.

We present the calculated and measured supercontinuum spectra of different waveguide widths with 100 pJ coupled pulse energy (coupled peak power of 1.1 kW) in Figs. 2(b) and 2(c), respectively. The measured output optical powers of the waveguides range from 1–2 mW (average power), depending on the waveguide widths. The theoretical supercontinuum is

calculated by solving the generalized nonlinear Schrödinger equation (gNLSE) [26,47]. We solve the gNLSE using the split-step Fourier method with an adaptive step-size algorithm, the details of which can be found in Ref. [36]. In our model, we include linear losses, waveguide dispersion, nonlinear phase shift, 3PA, steepening, as well as 3PA-induced free carrier absorption and dispersion [36] (Supplement 1). We simulate the evolution of our 85 fs Gaussian pulse at 3.06 µm along the waveguide length of 5 mm, with propagation loss of 2 dB/cm.

The measured spectra are in excellent agreement with the simulations, enabling full control over the geometrical dispersion design parameters. For the waveguide widths of 1.0–3.0 µm, the supercontinuum contains a dispersive wave with center wavelength that is lithographically tailored from 5.0–8.5 µm, as predicted by the engineered long-wavelength ZDW [Fig. 1(i)]. The longest wavelength dispersive wave is generated with the waveguide width of 2.40 µm [Fig. 2(d)], and covers the spectral bandwidth of 8.0–8.8 µm. We note that Si transmission drops at wavelengths larger than 8.8 µm (1130 cm⁻¹), preventing longer
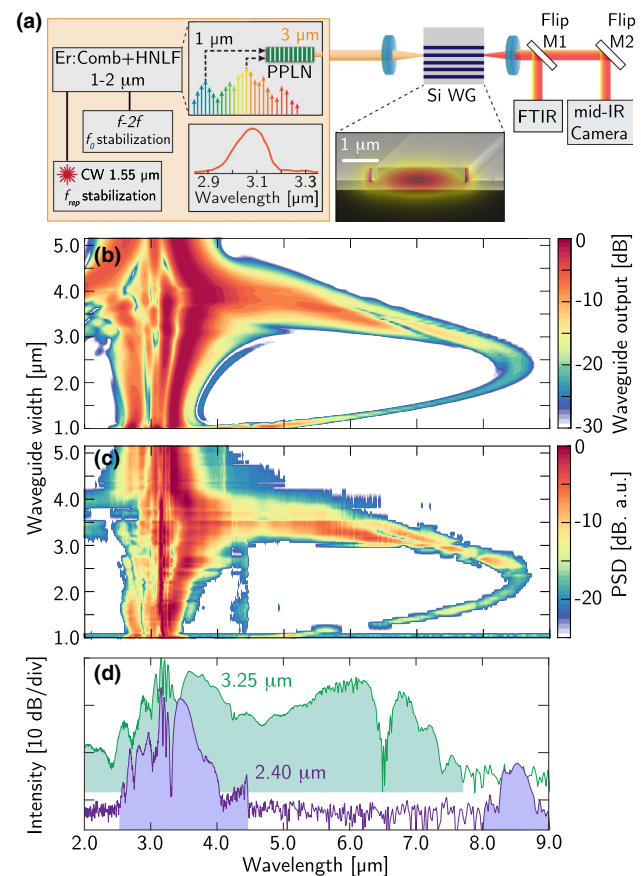

Fig. 2. Supercontinuum generation in the 5 mm long suspended Si waveguides. (a) Schematic of the experimental setup for pumping the Si waveguides. The 3.06 µm pump source is based on a 1550 nm Er:comb with f_0 and f_{rep} locking and DFG in a PPLN crystal. HNLF, highly nonlinear fiber; CW, continuous wave; Si WG, silicon waveguide; M1 and M2, gold mirrors. A zoomed-in, cross-sectional SEM of a suspended Si waveguide overlaid with a simulation of the 8 µm mode is also presented. The (b) calculated and (c) measured supercontinuum spectra of the waveguides. (d) Individual spectra generated with 3.25 and 2.40 µm wide waveguides, emphasizing the broadest generated bandwidth and the longest wavelength dispersive wave, respectively.

wavelength light generation due to absorption by the Si lattice phonon modes [48], not represented in our model. For wider waveguides (3.0–4.0 µm widths) the broad and flat anomalous dispersion profiles with near-zero values result in broad supercontinuum generation covering more than an octave. The broadest bandwidth is measured for the waveguide width of 3.25 µm, and it spans 2.0–7.7 µm [Fig. 2(d)]. This broadband spectrum of comb lines is suitable for spectroscopic study of a wide range of gas, liquid, and solid phase samples.

3. DUAL-COMB SPECTROSCOPY

Frequency comb lasers have been extensively utilized for spectroscopy applications in the IR. This includes complementing existing Fourier-transform spectrometers [49–52] as well as the development of alternative spectroscopy schemes such as direct frequency comb spectroscopy with a highly dispersive etalon [53–56], electro-optic sampling of the electric field [15,20,57], and dual-comb spectroscopy (DCS) [19,58–61].

DCS is an implementation of Fourier transform spectroscopy in which the interference of two frequency combs with slightly different repetition rates, f_{rep} and $f_{rep} + \delta f_{rep}$, maps the optical spectrum to the radio frequency domain [59]. Depending on the configuration, one or both combs pass through a sample and then interfere on a photodetector. In the time domain, an interference pattern is recorded whenever the pulses of the two combs overlap in time, generating a repetitive interferogram with period of $1/\delta f_{rep}$. The Fourier transform of this signal results in the optical spectrum of the dual-comb system with the imprinted sample absorption.

We use our waveguides in a dual-comb setup to demonstrate the coherence of the waveguide-generated light for DCS applications. The second comb in our DCS experiment is based on an Er:doped oscillator and intrapulse DFG in an orientation-patterned GaP (OP-GaP) crystal [19], generating ∼300 µW of optical power in the wavelength range of 4–17 µm. To better match the spectral bands, we add a short-pass filter (MgF_2 window) to the beam path of the OP-GaP comb, limiting its long-wavelength bandwidth to <9 µm. In addition, we place a 4.5 µm long-pass filter in the combined beam path of the two combs. The addition of these filters limits the spectral bandwidth of the dual-comb system to 4.5–8.8 µm. The seed 1550 nm light of both combs is self-referenced for f_0 stabilization using conventional f-to-$2f$ interferometers. In addition, using a 1550 nm cavity-stabilized continuous-wave laser, we stabilize repetition rates [Fig. 2(a)] at the ∼100 nHz level (at 1 s) with $\delta f_{rep} = 50$ Hz [19]. This results in the dual-comb interferogram periodicity of 20 ms. We present a sequence of five interferograms in
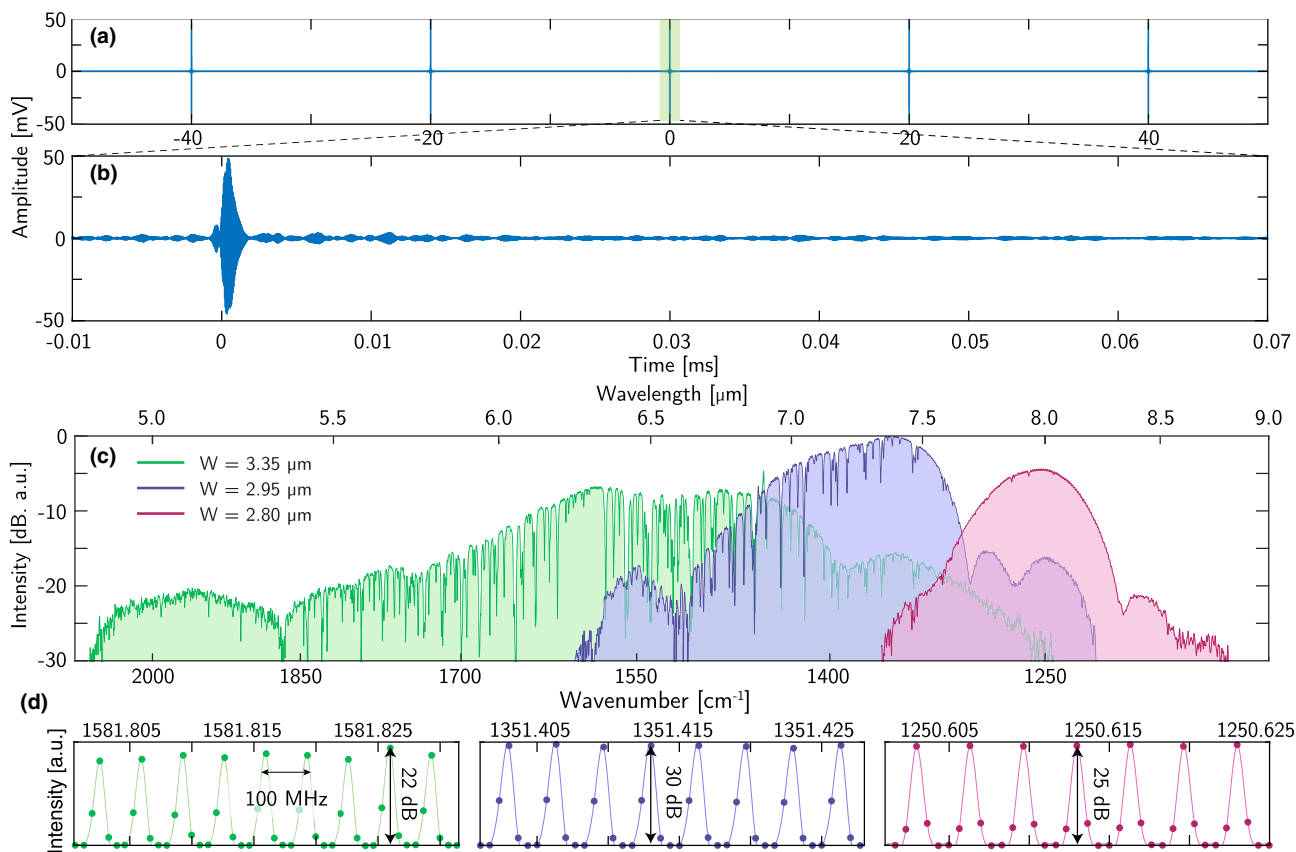

Fig. 3. Dual-comb interferograms and spectra. (a) Time-domain multi-heterodyne interferogram of the dual-comb system for the waveguide width of $W = 2.95$ µm. A sequence of five interferograms is shown with time separation of $1/\delta f_{rep} = 20$ ms. (b) Zoomed-in view of one of the interferograms, emphasizing the center-burst and trailing molecular free-induction decay oscillations of the atmospheric water absorption at the LWIR. (c) The frequency-domain dual-comb spectrum is calculated by taking an FFT of a single, averaged time-domain interferogram. Generated spectra for three waveguide widths of 2.80, 2.95, and 3.35 µm are presented, highlighting the spectral coverage from 4.9 to 8.80 µm. (d) A 0.025 cm^{-1} window of the dual-comb spectra in (c), presenting the 100 MHz spacing comb lines resolved with 22–30 dB extinction ratio. This is calculated by taking an FFT of the five periodic time-domain interferograms.

Fig. 3(a), measured in a 100 ms acquisition time window using the output of the 2.95 μm wide waveguide. The low amplitude noise and high mutual coherence of the stabilized lasers enable us to achieve the estimated time-domain signal-to-noise ratio (SNR) of 1200 after averaging 16,384 frames, corresponding to 27 min. Figure 3(b) presents a 80 μs window of one of the interferograms. The large oscillation near $t = 0$ s is the center-burst representing the spectral envelop of the dual-comb system. The trailing oscillations are molecular free-induction-decay [62] signatures of the atmospheric water absorption centered at ~6.25 μm (~1600 cm^{-1}).

We retrieve the optical spectrum by calculating the Fourier transform of the time-domain interferogram. Using three different waveguide widths of 3.35, 2.95, and 2.80 μm [Fig. 3(c)], our dual-comb setup covers the IR range of 4.9–8.8 μm (1130–2050 cm^{-1}) with spectral resolution of 100 MHz (0.0033 cm^{-1}). The broadest simultaneous bandwidth is measured using the 3.35 μm wide waveguide and it spans 4.9–8.0 μm (1250–2050 cm^{-1}), containing 2.7×10^5 comb lines. The highest spectral SNR is obtained using the 2.95 μm wide waveguide, while the waveguide width of 3.35 μm has the lowest measured SNR due to the broad bandwidth and the lower optical power per comb line generated by this device. For an averaging time of $\tau = 330$ s, we estimate the highest obtained SNR to be 180 over the 374 cm^{-1} spectral bandwidth. Normalized to a one second averaging time, we get SNR = 10 $\sqrt{\text{Hz}}$ at 100 MHz comb line resolution. Having a total of $M = 112,200$ comb lines, we calculate our DCS FOM as $M \times \text{SNR} = 1.1 \times 10^6 \sqrt{\text{Hz}}$ [63]. This is similar to the previously reported value for a dual-comb setup with two identically designed IR frequency combs based on intrapulse DFG in OP-GaP crystals [19], confirming the coherence of the nonlinear processes in the Si waveguides. Figure 3(d) presents zoomed-in views of the three spectra in Fig. 3(c), emphasizing the resolved

individual comb lines with the 100 MHz spacing. The comb lines are resolved with 22, 25, and 30 dB extinction ratios for waveguide widths of 3.35, 2.80, and 2.95 μm, respectively.

We utilize the waveguide-based dual-comb setup to study atmospheric water vapor from 1200–1600 cm^{-1}. Such analysis enables monitoring of controlled lab environments through the study of atmospheric pressures and water concentrations, measured in terms of volume-mixing ratio. Figure 4(a) presents the measured atmospheric water absorbance with 100 MHz comb line resolution. Data, presented in red, is compared to the HITRAN database [64], presented in blue and reflected about the x axis. We define absorbance as $A = \log_{10}(I/I_0)$, where I_0 and I are the calculated spectral baseline (Supplement 1) and measured spectrum, respectively. Our dual-comb setup has an atmospheric beam path of ~2 m, resulting in many saturated absorbance peaks. Hence, we only present and analyze the absorption data in three unsaturated regions of 1258–1272 cm^{-1}, 1340–1373 cm^{-1}, and 1588–1608 cm^{-1}. The data in these ranges are measured using 2.80, 2.95, and 3.35 μm wide waveguides, respectively.

We calculate the fit residuals as data minus the HITRAN model [Fig. 4(b)]. The calculated root-mean-square (RMS) of the residuals is 0.007 for the measurement ranges of 1258–1272 cm^{-1} and 1342–1373 cm^{-1}, emphasizing the excellent agreement between the DCS and HITRAN. This value increases for the 1588–1680 cm^{-1} range to 0.02 due to the lower optical power. Such excellent agreement between DCS measurements and the HITRAN database enables us to estimate the in-lab atmospheric pressure and volume-mixing ratio of the water content as 817 ± 41 mbar and 0.016 ± 0.002, respectively. These values agree well with the typical recorded values for the city of Boulder due to the area's higher elevation. A detailed explanation of this estimation is provided in Supplement 1.
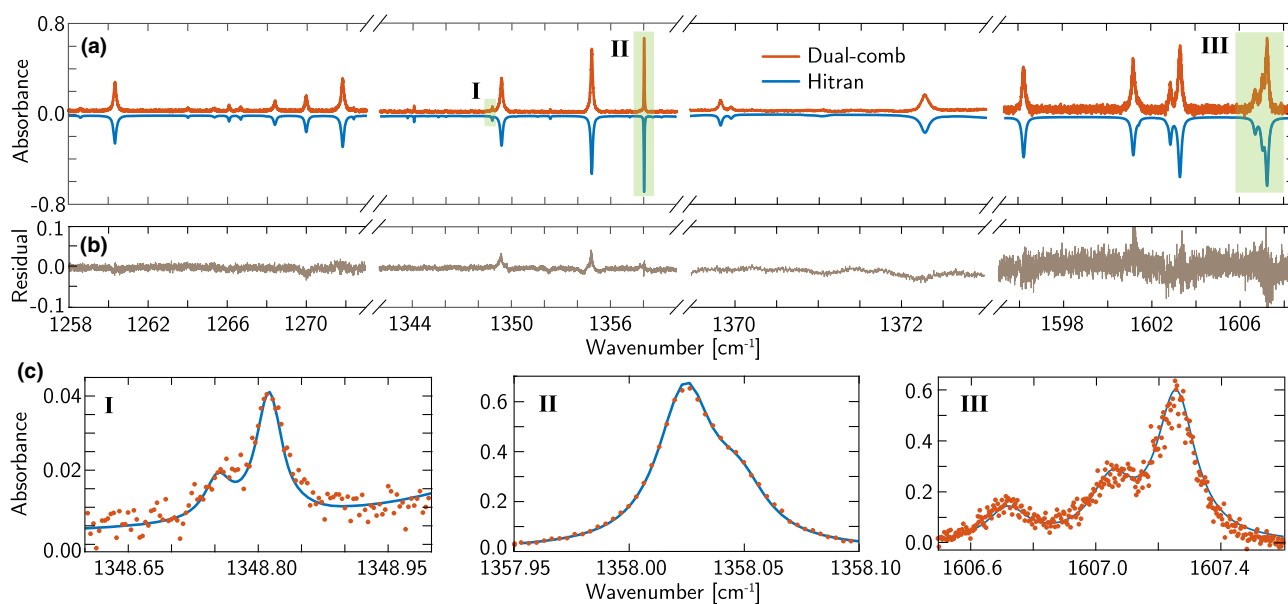

Fig. 4. Dual-comb measurement of the atmospheric water absorption. (a) Baseline-corrected DCS of the atmospheric water absorption with the 100 MHz (0.0033 cm^{-1}) comb line spacing resolution in the 1250–1610 cm^{-1} range (6.2–8.0 μm). The dual-comb data (red) is compared with the HITRAN database (blue, reflected about the x axis). Data is measured using 2.80, 2.95, and 3.35 μm wide waveguides. The HITRAN is fitted to the DCS data by a Voigt fitting algorithm to estimate Lorentzian and Gaussian lineshapes. (b) Difference between the data and the fit (residuals), showing excellent agreement between DCS and HITRAN within 1.5% uncertainty. The higher residuals at 1588–1610 cm^{-1} (5% error) are due to the lower optical power from the dual-comb system in this frequency range. (c) Zoomed-in view of the highlighted regions in (a).

To emphasize our high-DCS figure-of-merit, excellent frequency resolution, and low fitting uncertainty, we highlight three absorbance features in Fig. 4(a) and present their zoomed-in windows in Fig. 4(c). The high DCS FOM enables us to detect absorbance features of 10^{-2} levels [Fig. 4(c), panel I] which is similar to the levels achieved with FTIR spectrometers. Moreover, the fine comb-tooth spacing enables resolution of the narrow-linewidth features such as presented in Fig. 4(c), panel II, with FWHM ≈ 1.2 GHz (0.04 cm^{-1}). In a conventional FTIR spectrometer, a delay range of 3.0 m would be required to achieve the demonstrated 100 MHz spectral resolution. Despite the increased residual in the 1588–1608 cm^{-1} range, the measurement still agrees well with HITRAN [Fig. 4(c), panel III]. We can estimate the in-lab atmospheric pressure and water concentration by only comparing the HITRAN model to this data set. In this case, the atmospheric pressure and water content are calculated within 1.4% and 3% of the values estimated using the data from all waveguide widths, respectively.

We also measure the absorption spectrum of liquid-phase alcohols, leveraging the broadband and smooth waveguide spectra. Characterization of broad absorbers require spectral envelope stability over a broadband region to enable proper baseline measurement and subtraction [16]. The stability of our supercontinuum-generated frequency comb enables coherent averaging and measurement of large absorbance values. Moreover, to eliminate the effects of long-term, few-minute-timescale drifts we perform simultaneous measurement of the sample and reference spectra. In such a scheme, we use two liquid-nitrogen cooled mercury–cadmium–telluride (MCT) detectors at the two sides of the 50/50 beamsplitter that combines the IR combs [Fig. 5(a)]. The combined beams pass through a sample cell in one of the arms before being detected. In the other arm, the beam is sent directly to the detector as the reference measurement. Care is taken to have equal beam paths between the two arms to minimize the residual atmospheric absorption features after the baseline subtraction.

We choose isopropanol and methanol for liquid-phase spectroscopy because they are widely used for scientific and industrial applications. For our DCS demonstration, we use a 15 µm thick liquid sample cell to minimize the interaction length with the liquid and avoid saturated absorption. In liquid-phase spectroscopy, the absorbance lines are broadened to form a continuous spectrum, and 1 cm^{-1} spectral resolution is sufficient to resolve the features. We perform the liquid-phase DCS experiments with a resolution of 0.67 cm^{-1}, achieved via temporal apodization of the dual-comb interferogram to a 100 µs window. Figure 5(b) presents the sample and reference spectra of methanol (top panel) and isopropanol (bottom panel), measured using different waveguide widths for each sample.

We compare our baseline subtracted (Supplement 1) DCS data to measurements performed using a commercial FTIR operating with 1 cm^{-1} resolution in Figs. 5(c) and 5(d) for methanol and isopropanol, respectively. The DCS data is in excellent agreement with the FTIR spectrum, yielding a RMS residual value of 0.02. We note that the calculated residual levels are only limited by the uncorrected atmospheric water absorption contaminating the DCS data. Such agreement enables accurate analysis of the DCS spectra to assign the measured absorbance features to different molecular vibrational transitions (Supplement 1).
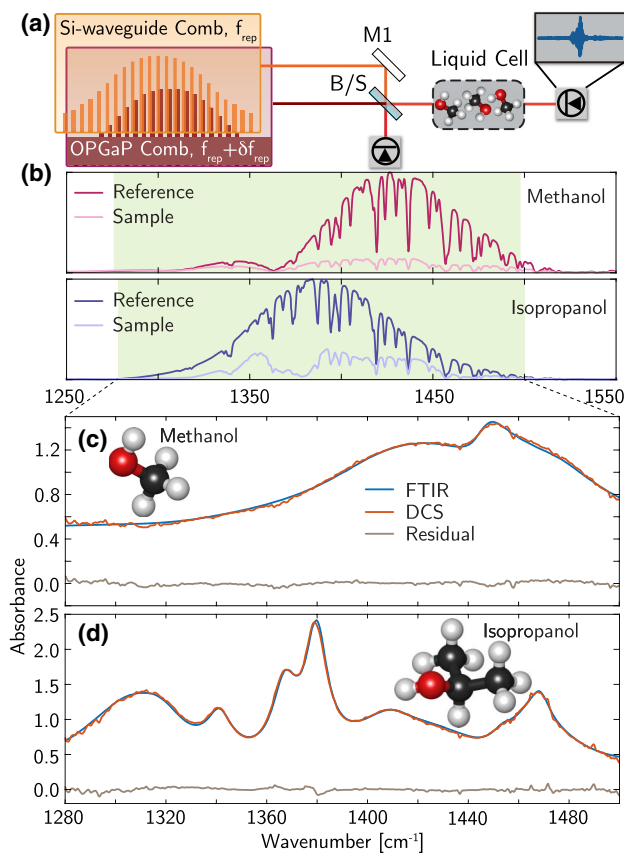

Fig. 5. Broadband DCS of liquid methanol and isopropanol. (a) Schematic diagram of the dual-comb setup for simultaneous measurement of the sample and reference spectra. M1, gold mirror; B/S, mid-IR beamsplitter. (b) Dual-comb spectra of the reference and sample for methanol (top panel) and isopropanol (bottom panel). The green shaded area is the region with sufficient SNR to calculate the absorbance of the liquid samples. The measured DCS absorbance of (c) methanol and (d) isopropanol are compared with FTIR measurements in the range of 1280–1500 cm^{-1}. The simultaneous reference and sample measurement, along with the smooth waveguide spectrum, enable broadbandwidth DCS of liquid samples.

While demonstrated for well-known alcohols, the bright waveguide-generated light and dual-comb measurement techniques we employ can be widely applied to other samples. The frequency range of 1200–1600 cm^{-1} enables access to C—H and O—H bending functional groups. This region of the IR provides stronger integrated absorption intensities and lower rovibrational density of states when compared with C—H stretching functional groups at 2000–3000 cm^{-1} (3–5 µm).

4. CONCLUSION AND SUMMARY

We introduced suspended Si waveguides as a versatile nonlinear photonic platform for spectral engineering of frequency combs across the mid-IR. By removing cladding absorption and reducing nonlinear losses in a straight nanophotonic waveguide, our platform achieves a spectral bandwidth unprecedented in other on-chip frequency comb systems. Our waveguide-generated frequency combs can be lithographically tailored across the optical bandwidth of 2.0–8.8 µm through coherent supercontinuum generation in multiple waveguide widths with milliwatt-scale

average power. We leverage precise dispersion engineering and mature fabrication to demonstrate efficient photonic-chip-based spectral engineering across a 116 THz bandwidth with a 100 pJ pump pulse energy. To the best of our knowledge, this is the first demonstration of nanophotonic-based frequency combs with such broadband spectra and milliwatt-scale average powers.

To demonstrate the coherence of the waveguide-generated light and its utility for DCS applications, we utilized our nonlinear devices in a dual-comb setup. We have achieved a DCS FOM of $1.1 \times 10^6 \sqrt{\text{Hz}}$, which is competitive with current state-of-the-art systems operating in the same spectral region. The smoothness of the generated spectra and our fine-comb-tooth spacing of 100 MHz (0.0033 cm^{-1}) enables probing of gas-phase narrow-linewidth absorbers as well as condensed-phase samples with broad absorption features. The DCS data have excellent agreement with the standard databases and FTIR measurements within less than 5% error.

Moreover, using the 3.25 μm wide waveguide as an example, only 1% of the generated optical power at 2 μm extends into the air trench underneath the waveguide core. This value, however, increases to 10%–16% for the wavelength range of 5.0–7.0 μm and to 22% for the longest-wavelength dispersive wave at 8.5 μm generated in the 2.40 μm wide waveguide. Such easy, on-chip access to the optical powers at wavelengths >5 μm presents the opportunity to integrate these devices with chip-based chemical delivery systems like microfluidic channels. In addition, if access to shorter wavelengths is desired, the waveguide can be tapered to narrower widths to extend the generated short-wavelength optical power into the trench. We envision the integration of this platform with high-repetition-rate sources, such as monolithic mode-locked lasers [1] and microresonator-based frequency combs [28,29], along with chemical delivery schemes for on-chip, parallel, multichannel *in situ* chemical studies and reaction monitoring.

See Supplement 1 for supporting content.

†These authors contributed equally to this work.

REFERENCES

1. T. D. Shoji, W. Xie, K. L. Silverman, A. Feldman, T. Harvey, R. P. Mirin, and T. R. Schibli, "Ultra-low-noise monolithic mode-locked solid-state laser," Optica **3**, 995–998 (2016).
2. N. Jornod, K. Gürel, V. J. Wittwer, P. Brochard, S. Hakobyan, S. Schilt, D. Waldburger, U. Keller, and T. Südmeyer, "Carrier-envelope offset frequency stabilization of a gigahertz semiconductor disk laser," Optica **4**, 1482–1487 (2017).
3. M. L. Davenport, S. Liu, and J. E. Bowers, "Integrated heterogeneous silicon/III-V mode-locked lasers," Photon. Res. **6**, 468–478 (2018).
4. D. R. Carlson, D. D. Hickstein, A. Lind, S. Droste, D. Westly, N. Nader, I. Coddington, N. R. Newbury, K. Srinivasan, S. A. Diddams, and S. B. Papp, "Self-referenced frequency combs using high-efficiency silicon-nitride waveguides," Opt. Lett. **42**, 2314–2317 (2017).
5. Y. Okawachi, M. Yu, J. Cardenas, X. Ji, A. Klenner, M. Lipson, and A. L. Gaeta, "Carrier envelope offset detection via simultaneous supercontinuum and second-harmonic generation in a silicon nitride waveguide," Opt. Lett. **43**, 4627–4630 (2018).
6. Y. Okawachi, M. Yu, J. Cardenas, X. Ji, M. Lipson, and A. L. Gaeta, "Coherent, directional supercontinuum generation," Opt. Lett. **42**, 4466–4469 (2017).
7. D. Waldburger, A. S. Mayer, C. G. E. Alfieri, J. Nürnberg, A. R. Johnson, X. Ji, A. Klenner, Y. Okawachi, M. Lipson, A. L. Gaeta, and U. Keller, "Tightly locked optical frequency comb from a semiconductor disk laser," Opt. Express **27**, 1786–1797 (2019).
8. S. A. Diddams, D. J. Jones, J. Ye, S. T. Cundiff, J. L. Hall, J. K. Ranka, R. S. Windeler, R. Holzwarth, T. Udem, and T. W. Hänsch, "Direct link between microwave and optical frequencies with a 300 THz femtosecond laser comb," Phys. Rev. Lett. **84**, 5102–5105 (2000).
9. D. J. Jones, S. A. Diddams, J. K. Ranka, A. Stentz, R. S. Windeler, J. L. Hall, and S. T. Cundiff, "Carrier-envelope phase control of femtosecond mode-locked lasers and direct optical frequency synthesis," Science **288**, 635–639 (2000).
10. T. Udem, S. A. Diddams, K. R. Vogel, C. W. Oates, E. A. Curtis, W. D. Lee, W. M. Itano, R. E. Drullinger, J. C. Bergquist, and L. Hollberg, "Absolute frequency measurements of the Hg2+ and Ca optical clock transitions with a femtosecond laser," Phys. Rev. Lett. **86**, 4996–4999 (2001).
11. S. T. Cundiff and J. Ye, "Colloquium: Femtosecond optical frequency combs," Rev. Mod. Phys. **75**, 325–342 (2003).
12. A. Schliesser, N. Picqué, and T. W. Hansch, "Mid-infrared frequency combs," Nat. Photonics **6**, 440–449 (2012).
13. I. Sorokina and K. Vodopyanov, *Solid-State Mid-Infrared Laser Sources*, 1st ed., Vol. **89** of Topics in Applied Physics, (Springer, 2003).
14. M. Ebrahim-Zadeh and I. T. Sorokina, eds., *Mid-Infrared Coherent Sources and Applications*, NATO Science for Peace and Security Series B: Physics and Biophysics (Springer Netherlands, 2008).
15. A. Sell, R. Scheu, A. Leitenstorfer, and R. Huber, "Field-resolved detection of phase-locked infrared transients from a compact Er:fiber system tunable between 55 and 107 THz," Appl. Phys. Lett. **93**, 251107 (2008).
16. G. Ycas, F. R. Giorgetta, E. Baumann, I. Coddington, D. Herman, S. A. Diddams, and N. R. Newbury, "High-coherence mid-infrared dual-comb spectroscopy spanning 2.6 to 5.2 μm," Nat. Photonics **12**, 202–208 (2018).
17. A. V. Muraviev, V. O. Smolski, Z. E. Loparo, and K. L. Vodopyanov, "Massively parallel sensing of trace molecules and their isotopologues with broadband subharmonic mid-infrared frequency combs," Nat. Photonics **12**, 209–214 (2018).
18. A. J. Lind, A. Kowligy, H. Timmers, F. C. Cruz, N. Nader, M. C. Silfies, T. K. Allison, and S. A. Diddams, "χ^2 mid-infrared frequency comb generation and stabilization with few-cycle pulses," arXiv:1811.02604 (2018).
19. H. Timmers, A. Kowligy, A. Lind, F. C. Cruz, N. Nader, M. Silfies, G. Ycas, T. K. Allison, P. G. Schunemann, S. B. Papp, and S. A. Diddams, "Molecular fingerprinting with bright, broadband infrared frequency combs," Optica **5**, 727–732 (2018).
20. A. S. Kowligy, H. Timmers, A. J. Lind, U. Elu, F. C. Cruz, P. G. Schunemann, J. Biegert, and S. A. Diddams, "Infrared electric field sampled frequency comb spectroscopy," Sci. Adv. **5**, eaaw8794 (2019).
21. L. C. Sinclair, I. Coddington, W. C. Swann, G. B. Rieker, A. Hati, K. Iwakuni, and N. R. Newbury, "Operation of an optically coherent frequency comb outside the metrology lab," Opt. Express **22**, 6996–7006 (2014).
22. J. Chiles, S. Khan, J. Ma, and S. Fathpour, "High-contrast, all-silicon waveguiding platform for ultra-broadband mid-infrared photonics," Appl. Phys. Lett. **103**, 151106 (2013).
23. R. Kou, T. Hatakeyama, J. Horng, J.-H. Kang, Y. Wang, X. Zhang, and F. Wang, "Mid-IR broadband supercontinuum generation from a suspended silicon waveguide," Opt. Lett. **43**, 1387–1390 (2018).
24. K. S. Kim, R. H. Stolen, W. A. Reed, and K. W. Quoi, "Measurement of the nonlinear index of silica-core and dispersion-shifted fibers," Opt. Lett. **19**, 257–259 (1994).

25. X. Gai, Y. Yu, B. Kuyken, P. Ma, S. J. Madden, J. Van Campenhout, P. Verheyen, G. Roelkens, R. Baets, and B. Luther-Davies, "Nonlinear absorption and refraction in crystalline silicon in the mid-infrared," Laser Photon. Rev. 7, 1054–1064 (2013).

26. R. K. W. Lau, M. R. E. Lamont, A. G. Griffith, Y. Okawachi, M. Lipson, and A. L. Gaeta, "Octave-spanning mid-infrared supercontinuum generation in silicon nanowaveguides," Opt. Lett. 39, 4518–4521 (2014).

27. B. Kuyken, T. Ideguchi, S. Holzner, M. Yan, T. W. Hansch, J. Van Campenhout, P. Verheyen, S. Coen, F. Leo, R. Baets, G. Roelkens, and N. Picqué, "An octave-spanning mid-infrared frequency comb generated in a silicon nanophotonic wire waveguide," Nat. Commun. 6, 6310 (2015).

28. M. Yu, Y. Okawachi, A. G. Griffith, M. Lipson, and A. L. Gaeta, "Microresonator-based high-resolution gas spectroscopy," Opt. Lett. 42, 4442–4445 (2017).

29. M. Yu, Y. Okawachi, A. G. Griffith, N. Picqué, M. Lipson, and A. L. Gaeta, "Silicon-chip-based mid-infrared dual-comb spectroscopy," Nat. Commun. 9, 1869 (2018).

30. D. D. Hickstein, H. Jung, D. R. Carlson, A. Lind, I. Coddington, K. Srinivasan, G. G. Ycas, D. C. Cole, A. Kowligy, C. Fredrick, S. Droste, E. S. Lamb, N. R. Newbury, H. X. Tang, S. A. Diddams, and S. B. Papp, "Ultrabroadband supercontinuum generation and frequency-comb stabilization using on-chip waveguides with both cubic and quadratic nonlinearities," Phys. Rev. Appl. 8, 014025 (2017).

31. A. S. Kowligy, A. Lind, D. D. Hickstein, D. R. Carlson, H. Timmers, N. Nader, F. C. Cruz, G. Ycas, S. B. Papp, and S. A. Diddams, "Mid-infrared frequency comb generation via cascaded quadratic nonlinearities in quasi-phase-matched waveguides," Opt. Lett. 43, 1678–1681 (2018).

32. H. Guo, C. Herkommer, A. Billat, D. Grassani, C. Zhang, M. H. P. Pfeiffer, W. Weng, C.-S. Brès, and T. J. Kippenberg, "Mid-infrared frequency comb via coherent dispersive wave generation in silicon nitride nanophotonic waveguides," Nat. Photonics 12, 330–335 (2018).

33. D. Grassani, E. Tagkoudi, H. Guo, C. Herkommer, F. Yang, T. J. Kippenberg, and C.-S. Brès, "Mid infrared gas spectroscopy using efficient fiber laser driven photonic chip-based supercontinuum," Nat. Commun. 10, 1553 (2019).

34. R. Shankar, I. Bulu, and M. Lončar, "Integrated high-quality factor silicon-on-sapphire ring resonators for the mid-infrared," Appl. Phys. Lett. 102, 051108 (2013).

35. N. Singh, D. D. Hudson, Y. Yu, C. Grillet, S. D. Jackson, A. Casas-Bedoya, A. Read, P. Atanackovic, S. G. Duvall, S. Palomba, B. Luther-Davies, S. Madden, D. J. Moss, and B. J. Eggleton, "Midinfrared supercontinuum generation from 2 to 6 μm in a silicon nanowire," Optica 2, 797–802 (2015).

36. N. Nader, D. L. Maser, F. C. Cruz, A. Kowligy, H. Timmers, J. Chiles, C. Fredrick, D. A. Westly, S. W. Nam, R. P. Mirin, J. M. Shainline, and S. Diddams, "Versatile silicon-waveguide supercontinuum for coherent mid-infrared spectroscopy," APL Photon. 3, 036102 (2018).

37. M. Sinobad, C. Monat, B. Luther-davies, P. Ma, S. Madden, D. J. Moss, A. Mitchell, D. Allioux, R. Orobtchouk, S. Boutami, J.-M. Hartmann, J.-M. Fedeli, and C. Grillet, "Mid-infrared octave spanning supercontinuum generation to 8.5 μm in silicon-germanium waveguides," Optica 5, 360–366 (2018).

38. Y. Yu, X. Gai, P. Ma, K. Vu, Z. Yang, R. Wang, D.-Y. Choi, S. Madden, and B. Luther-Davies, "Experimental demonstration of linearly polarized 2-10 μm supercontinuum generation in a chalcogenide rib waveguide," Opt. Lett. 41, 958–961 (2016).

39. M. Sinobad, A. D. Torre, B. Luther-Davis, P. Ma, S. Madden, S. Debbarma, K. Vu, D. J. Moss, A. Mitchell, J.-M. Hartmann, J.-M. Fedeli, C. Monat, and C. Grillet, "Dispersion trimming for mid-infrared supercontinuum generation in a hybrid chalcogenide/silicon-germanium waveguide," J. Opt. Soc. Am. B 36, A98–A104 (2019).

40. S. A. Miller, M. Yu, X. Ji, A. G. Griffith, J. Cardenas, A. L. Gaeta, and M. Lipson, "Low-loss silicon platform for broadband mid-infrared photonics," Optica 4, 707–712 (2017).

41. J. Chiles, N. Nader, E. J. Stanton, D. Herman, G. Moody, J. Zhu, J. C. Skehan, B. Guha, A. Kowligy, J. T. Gopinath, K. Srinivasan, S. A. Diddams, I. Coddington, N. R. Newbury, J. M. Shainline, S. W. Nam, and R. P. Mirin, "Multi-functional integrated photonics in the mid-infrared with suspended AlGaAs on silicon," arXiv:1905.01380 (2019).

42. X. Jiang, H. Wu, and D. Dai, "Low-loss and low-crosstalk multimode waveguide bend on silicon," Opt. Express 26, 17680–17689 (2018).

43. W. Bogaerts and S. K. Selvaraja, "Compact single-mode silicon hybrid rib/strip waveguide with adiabatic bends," IEEE Photon. J. 3, 422–432 (2011).

44. F. C. Cruz, D. L. Maser, T. Johnson, G. Ycas, A. Klose, F. R. Giorgetta, I. Coddington, and S. A. Diddams, "Mid-infrared optical frequency combs based on difference frequency generation for molecular spectroscopy," Opt. Express 23, 26814–26824 (2015).

45. F. Gholami, S. Zlatanovic, A. Simic, L. Liu, D. Borlaug, N. Alic, M. P. Nezhad, Y. Fainman, and S. Radic, "Third-order nonlinearity in silicon beyond 2350 nm," Appl. Phys. Lett. 99, 081102 (2011).

46. Q. Lin, J. Zhang, G. Piredda, R. W. Boyd, P. M. Fauchet, and G. P. Agrawal, "Dispersion of silicon nonlinearities in the near infrared region," Appl. Phys. Lett. 91, 021111 (2007).

47. Q. Lin, O. J. Painter, and G. P. Agrawal, "Nonlinear optical phenomena in silicon waveguides: Modeling and applications," Opt. Express 15, 16604–16644 (2007).

48. F. A. Johnson, "Lattice absorption bands in silicon," Proc. Phys. Soc. 73, 265–272 (1959).

49. J. Mandon, G. Guelachvili, and N. Picqué, "Fourier transform spectroscopy with a laser frequency comb," Nat. Photonics 3, 99 (2009).

50. B. Spaun, P. B. Changala, D. Patterson, B. J. Bjork, O. H. Heckl, J. M. Doyle, and J. Ye, "Continuous probing of cold complex molecules with infrared frequency comb spectroscopy," Nature 533, 517 (2016).

51. B. J. Bjork, T. Q. Bui, O. H. Heckl, P. B. Changala, B. Spaun, P. Heu, D. Follman, C. Deutsch, G. D. Cole, M. Aspelmeyer, M. Okumura, and J. Ye, "Direct frequency comb measurement of OD + CO → DOCO kinetics," Science 354, 444–448 (2016).

52. P. B. Changala, M. L. Weichman, K. F. Lee, M. E. Fermann, and J. Ye, "Rovibrational quantum state resolution of the C$_{60}$ fullerene," Science 363, 49–54 (2019).

53. S. A. Diddams, L. Hollberg, and V. Mbele, "Molecular fingerprinting with the resolved modes of a femtosecond laser frequency comb," Nature 445, 627 (2007).

54. L. Nugent-Glandorf, T. Neely, F. Adler, A. J. Fleisher, K. C. Cossel, B. Bjork, T. Dinneen, J. Ye, and S. A. Diddams, "Mid-infrared virtually imaged phased array spectrometer for rapid and broadband trace gas detection," Opt. Lett. 37, 3285–3287 (2012).

55. A. J. Fleisher, B. J. Bjork, T. Q. Bui, K. C. Cossel, M. Okumura, and J. Ye, "Mid-infrared time-resolved frequency comb spectroscopy of transient free radicals," J. Phys. Chem. Lett. 5, 2241–2246 (2014).

56. K. Iwakuni, T. Q. Bui, J. F. Niedermeyer, T. Sukegawa, and J. Ye, "Comb-resolved spectroscopy with immersion grating in long-wave infrared," Opt. Express 27, 1911–1921 (2019).

57. A. Bartels, R. Cerna, C. Kistner, A. Thoma, F. Hudert, C. Janke, and T. Dekorsy, "Ultrafast time-domain spectroscopy based on high-speed asynchronous optical sampling," Rev. Sci. Instrum. 78, 035107 (2007).

58. F. Keilmann, C. Gohle, and R. Holzwarth, "Time-domain mid-infrared frequency-comb spectrometer," Opt. Lett. 29, 1542–1544 (2004).

59. I. Coddington, N. Newbury, and W. Swann, "Dual-comb spectroscopy," Optica 3, 414–426 (2016).

60. O. Kara, L. Maidment, T. Gardiner, P. G. Schunemann, and D. T. Reid, "Dual-comb spectroscopy in the spectral fingerprint region using OPGaP optical parametric oscillators," Opt. Express 25, 32713–32721 (2017).

61. M. L. Weichman, P. B. Changala, J. Ye, Z. Chen, M. Yan, and N. Picqué, "Broadband molecular spectroscopy with optical frequency combs," J. Mol. Spectrosc. 355, 66–78 (2019).

62. I. Coddington, W. C. Swann, and N. R. Newbury, "Time-domain spectroscopy of molecular free-induction decay in the infrared," Opt. Lett. 35, 1395–1397 (2010).

63. N. R. Newbury, I. Coddington, and W. Swann, "Sensitivity of coherent dual-comb spectroscopy," Opt. Express 18, 7929–7945 (2010).

64. I. Gordon, L. Rothman, C. Hill, R. Kochanov, Y. Tan, P. Bernath, M. Birk, V. Boudon, A. Campargue, K. Chance, B. Drouin, J.-M. Flaud, R. Gamache, J. Hodges, D. Jacquemart, V. Perevalov, A. Perrin, K. Shine, M.-A. Smith, J. Tennyson, G. Toon, H. Tran, V. Tyuterev, A. Barbe, A. Császár, V. Devi, T. Furtenbacher, J. Harrison, J.-M. Hartmann, A. Jolly, T. Johnson, T. Karman, I. Kleiner, A. Kyuberis, J. Loos, O. Lyulin, S. Massie, S. Mikhailenko, N. Moazzen-Ahmadi, H. Müller, O. Naumenko, A. Nikitin, O. Polyansky, M. Rey, M. Rotger, S. Sharpe, K. Sung, E. Starikova, S. Tashkun, J. V. Auwera, G. Wagner, G. Wilzewski, P. Wcisło, S. Yu, and E. Zak, "The HITRAN2016 molecular spectroscopic database," J. Quant. Spectrosc. Radiat. Transfer 203, 3–69 (2017).